

# Observing patchy reionization with future CMB polarization experiments

A. Roy,<sup>a</sup> A. Lapi,<sup>a,b,c</sup> D. Spergel,<sup>d,e</sup> C. Baccigalupi<sup>a,b,c</sup>

<sup>a</sup>SISSA, Via Bonomea 265, 34136 Trieste, Italy

<sup>b</sup>INFN-Sezione di Trieste, via Valerio 2, 34127 Trieste, Italy

<sup>c</sup>INAF-Osservatorio Astronomico di Trieste, via Tiepolo 11, 34131 Trieste, Italy

<sup>d</sup>Department of Astrophysical Sciences, Princeton University, Princeton, NJ 08544, USA

<sup>e</sup>Center for Computational Astrophysics, Flatiron Institute, 162 5th Ave, New York, NY 10003, USA

E-mail: [aroy@sissa.it](mailto:aroy@sissa.it), [lapi@sissa.it](mailto:lapi@sissa.it), [dns@astro.princeton.edu](mailto:dns@astro.princeton.edu), [bacci@sissa.it](mailto:bacci@sissa.it)

**Abstract.** We study the signal from patchy reionization in view of the future high accuracy polarization measurements of the Cosmic Microwave Background (CMB). We implement an extraction procedure of the patchy reionization signal analogous to CMB lensing. We evaluate the signal to noise ratio (SNR) for the future Stage IV (S4) CMB experiment. The signal has a broad peak centered on the degree angular scales, with a long tail at higher multipoles. The CMB S4 experiment can effectively constrain the properties of reionization by measuring the signal on degree scales. The signal amplitude depends on the properties of the structure determining the reionization morphology. We describe bubbles having radii distributed log-normally. The expected S/N is sensitive to the mean bubble radius:  $\bar{R} = 5$  Mpc implies  $S/N \approx 4$ ,  $\bar{R} = 10$  Mpc implies  $S/N \approx 20$ . The spread of the radii distribution strongly affects the integrated SNR, that changes by a factor of  $10^2$  when  $\sigma_{\ln r}$  goes from  $\ln 2$  to  $\ln 3$ . Future CMB experiments will thus place important constraints on the physics of reionization.

**Keywords:** galaxy evolution — high redshift galaxies — reionization — CMBR polarisation

---

## Contents

<b>1</b>	<b>Introduction</b>	<b>1</b>
<b>2</b>	<b>Realistic Models of Reionization</b>	<b>3</b>
2.1	SFR functions	3
2.2	Cosmic star formation rate density	4
2.3	Reionization history	5
<b>3</b>	<b>CMB effects from Reionization</b>	<b>10</b>
3.1	Sky-averaged effect	10
3.2	Patchy Reionization	13
<b>4</b>	<b>Reconstruction of <math>\tau</math> along the line of sight</b>	<b>16</b>
<b>5</b>	<b>Detectability of the reionization angular power spectrum through <math>\tau</math> reconstruction in S4 CMB experiments</b>	<b>17</b>
5.1	Dependence on $\bar{\tau}$	18
5.2	Dependence on $\bar{R}$ and $\sigma_{lnr}$	18
<b>6</b>	<b>Summary and Outlook</b>	<b>22</b>

---

## 1 Introduction

Ultraviolet radiation from first sources ionizes the Inter-Galactic Medium (IGM) and alters the thermal, ionization and chemical properties of the gas. The reionization optical depth  $\tau$ , weighting Thomson cross section along the line of sight, represents a most important characterization of the effect. Through the measurements of large-scale  $E$  mode polarization in the Cosmic Microwave Background (CMB) anisotropies ("reionization bump"), the Wilkinson Microwave Anisotropy Probe (WMAP) has constrained the sky average optical depth to be  $0.089 \pm 0.014$  [36]; more recently, the Planck satellite, by combining data ranging from 30 to 353 GHz in polarization, reported a lower value,  $\tau = 0.058 \pm 0.012$  [69].

Accurate  $\tau$  measurements are crucial for breaking degeneracies with the amplitude of the primordial scalar perturbations  $A_s$  in order to infer the dependence of the primordial power with physical scales. However, a precise astrophysical knowledge of the reionization process is necessary for interpreting and exploiting the  $\tau$  measurements expected from future CMB polarization experiments. Most important targets of these efforts are represented by the  $B$ -modes of CMB polarization from cosmological Gravitational Waves (GWs) and Gravitational Lensing (GL). Currently the POLARBEAR/Simons Array [83, 84], BICEP<sup>1</sup>3 [2], ACTpol<sup>2</sup>[51], SPT 3G<sup>3</sup>[8], SPIDER<sup>4</sup> [26], EBEX<sup>5</sup> [72] and others<sup>6</sup> are searching these signals. In the near future the Simons Observatory <sup>7</sup> will be observing from the Atacama desert,

---

<sup>1</sup>Background Imaging of Cosmic Extragalactic Polarization, [www.cfa.harvard.edu/CMB/bicep3](http://www.cfa.harvard.edu/CMB/bicep3)

<sup>2</sup>Atacama Cosmology Telescope (polarization sensitive), <https://act.princeton.edu/>

<sup>3</sup>South Pole Telescope (third generation), <https://pole.uchicago.edu/>

<sup>4</sup><https://spider.princeton.edu>

<sup>5</sup>The E and B Experiment, <http://groups.physics.umn.edu/cosmology/ebex/>

<sup>6</sup>See [lambda.gsfc.nasa.gov](http://lambda.gsfc.nasa.gov) for a complete list of operating and planned CMB experiments.

<sup>7</sup><https://simonsobservatory.org>

paving the way to a network of ground based systems equipped with  $10^4$  detectors, which will represent the Stage-IV (S4) phase of ground based CMB experiment.

The detection of almost complete Ly $\alpha$  absorption in the spectra of distant quasars may suggest that the end of reionization occurred around  $z \approx 6$  [24]. Recent data on the evolution of Ly $\alpha$  optical depth show a sharp increase for redshift  $z$  larger than 6 – 7. A similar conclusion is supported by the study of line of sight variations in the IGM Ly $\alpha$  optical depth [7]. Moreover, the Ly $\alpha$  transmission profile of the highest-redshift quasar (Quasi-Stellar Objects, QSO) ULAS J112001.48+064124.3 at  $z \sim 7.1$  is strikingly different from that of two lower redshift  $z \sim 6.3 - 6.4$  counterparts detected in the Sloan Digital Sky Survey (SDSS<sup>8</sup>). It features a measured near-zone radius of  $\sim 1.9$  Mpc, a factor of  $\sim 3$  smaller than it is typical for QSOs at  $z \sim 6 - 6.5$  [61], suggesting higher- $z$  QSOs live in an IGM whose HI fraction is much higher. High redshift GRBs with their bright afterglow can be also exploited as probes of cosmic reionization, dispensing with some of the complications inherent to QSO observations. Extreme drop off in transmission profile of GRB140515A at  $z \approx 6.3$  places an upper limit on HI fraction at these redshift [15, 85]. Several studies support the picture that first galaxies in the Universe are the main source of reionization [5, 44, 74] but the morphology of the reionization process is still poorly understood. Numerical simulations as well as analytical studies suggest that ionization fraction is spatially inhomogeneous [5, 31, 48]. Reionization sources basically first ionize the surrounding IGM by producing ionized bubbles around them and later they grow and merge with each other [30, 66]. Patchy reionization produces different scattering histories along different line of sights so that the value of  $\tau$  varies with the direction. Patchy reionization also generate kinetic Sunyaev Zeldovich (kSZ) signal due to the peculiar motion of ionized bubbles along the line of sight [40, 63]. In the near future it will be possible to detect patchy kSZ signal and separating that from other secondary anisotropies in the CMB, by exploiting an accurate astrophysical modelling [80].

In this paper we study the capability of future CMB experiments concerning the reconstruction and understanding of the reionization process, by probing not only the sky averaged reionization history, but also the accessible information regarding its morphology through the dependence on the line of sight. That would provide invaluable insight into the reionization process which would open unprecedented windows on the astrophysical processes responsible for the EoR, but also allowing to reconstruct the overall behavior of cosmology at those epochs.

The paper is organized as follows: in Section 2 we discuss a realistic model of reionization based on recent determination of the star formation rate functions. In Section 3 we study the effects of reionization on the CMB. In Section 4 we implement the reconstruction method first introduced by Dvorkin & Smith [22] and forecast the capabilities of future CMB experiments with specifications corresponding to S4 to detect patchy reionization. In Section 5 we summarize our findings. Throughout this work we assume flat  $\Lambda$ CDM cosmology with parameters  $h = 0.677$ ,  $\Omega_b h^2 = 0.02230$ ,  $\Omega_c h^2 = 0.1188$ ,  $\Omega_\Lambda = 0.6911$ ,  $n_s = 0.9667$ ,  $A_s = 2.142 \times 10^{-9}$ , derived from the combinations of Planck TT,TE,EE,LowP+Lensing+Ext [68]. Stellar masses and luminosities of galaxies are based on a Chabrier initial mass function [14].

---

<sup>8</sup>[www.sdss.org](http://www.sdss.org)

## 2 Realistic Models of Reionization

The section describes our model of reionization based on the assumption that star-forming galaxies are the primary source of ionizing photons.

### 2.1 SFR functions

In this paper, we assume the Mancuso et al. [55, 56] and Lapi et al. [44] models of cosmological star formation history. These are based on analyses of recent dust-corrected UV, far-IR and radio data (see figure 1).

For galaxies with relatively low star formation rates ( $\dot{M}_\star \lesssim 30 M_\odot \text{ yr}^{-1}$ ), UV observations are the most important tracers of the SFR. Dust emission is mainly due to the diffuse (cirrus) dust component and attenuation is mild. Thus UV data extending down to a magnitude  $M_{\text{UV}} \approx -17$  have been dust-corrected according to the local empirical relation between the UV slope  $\beta_{\text{UV}}$  and the IR-to-UV luminosity ratio IRX [see 60], that is also routinely exploited for high-redshift galaxies [see 9–12]. A Meurer/Calzetti prescription has been adopted, but the determination of the SFR functions is only marginally affected at the faint end by choosing a different extinction law, like for example the Small Magellanic Cloud (SMC) one.

For galaxies with relatively higher star formation rates, far-IR and radio data are the most important tracers as dust emission is largely dominated by molecular clouds and the UV dust corrections are large and uncertain [see 17, 23, 28, 71, 79]. Interestingly, the shape of the SFR function for  $\dot{M}_\star \gtrsim 10^2 M_\odot \text{ yr}^{-1}$ , which so far has been probed only indirectly at  $z \gtrsim 4$  due to sensitivity limits in current far-IR surveys, is found to agree out to  $z \lesssim 6$  with the constraints from the recent VLA-COSMOS radio survey [see 64] and from the few individual galaxies detected at  $z \gtrsim 5$  with ALMA and SMA [see 73, 89].

The luminosity  $L$  has been converted into the SFR  $\dot{M}_\star$  using  $\log \dot{M}_\star / M_\odot \text{ yr}^{-1} \approx -9.8 + \log L / L_\odot$ , a good approximation both for far-IR and (intrinsic) UV luminosities, as expected on energy conservation arguments, under the assumption of a Chabrier’s IMF. Note that actually this conversion factor depends on the star formation history, and specifically on duration and age of the burst [see 13, 23]; the standard value adopted here is the average for a continuous star formation over 100 Myr, the age at which 90% of emission has been contributed [see 41, their table 1].

The SFR function can be described as a smooth Schechter function

$$\frac{dN}{d \log \dot{M}_\star}(\dot{M}_\star, z) = \mathcal{N}(z) \left[ \frac{\dot{M}_\star}{\dot{M}_{\star,c}(z)} \right]^{1-\alpha(z)} e^{-\dot{M}_\star / \dot{M}_{\star,c}(z)}, \quad (2.1)$$

with three parameters: the overall normalization  $\mathcal{N}$ , the characteristic SFR  $\dot{M}_{\star,c}$  and the faint end slope  $\alpha$ . The redshift evolution for each parameter  $p(z)$  of the Schechter function has been described as a third-order polynomial in log-redshift  $p(z) = p_0 + p_1 \xi + p_2 \xi^2 + p_3 \xi^3$ , with  $\xi = \log(1+z)$ . The values of the parameters  $\{p_i\}$  are reported in Table 1 of Lapi et al. [44]. In Figure 1 dashed lines refer to the (dust-corrected) UV-inferred SFR functions while solid line to the global (UV+far-IR/radio) SFR functions. The behavior of the normalization  $\mathcal{N}$  and of the characteristic SFR  $\dot{M}_{\star,c}$  highlights that UV surveys tend to pick up many galaxies with low SFR, while far-IR surveys also select less numerous galaxies with higher SFR; this mirrors the fact that high SFRs are usually associated to large dust abundance. The evolution with redshift of these parameters shows that most of the SFR occurs in dusty galaxies around redshift  $z \approx 2$  (cf. also Figure 2); on the other hand, toward high redshift  $z \gtrsim 6$  the dust

content progressively decreases and UV surveys become more effective in selecting the typical population of star forming galaxies. For the purpose of this paper, the high-redshift evolution is most relevant.

Mancuso et al. [55, 56] and Lapi et al. [44] validate the SFR functions against independent datasets, including integrated galaxy number counts at significative far-IR/(sub)mm/radio wavelengths, counts/redshift distributions of strongly gravitationally-lensed galaxies, stellar mass function via the continuity equation, main sequence of star-forming galaxies, and even associated AGN statistics. In particular, the analysis of the main sequence for high-redshift galaxies and AGNs presented in Mancuso et al. [57] and Lapi et al. (2017b) highlights that the current data can be consistently interpreted in terms of an in situ coevolution scenario for star formation and black hole accretion, envisaging these as local, time coordinated processes.

Since faint galaxies are likely the source of much of the ionizing background, we need to extrapolate the SFR to well beyond the magnitude limit of the current blank field surveys  $M_{\text{UV}} \approx -17$  (corresponding to SFR  $\dot{M}_\star \approx$  a few  $10^{-1} M_\odot \text{ yr}^{-1}$ ) down to  $M_{\text{UV}} \approx -13$  (corresponding to SFR  $\dot{M}_\star \approx$  a few  $10^{-2} M_\odot \text{ yr}^{-1}$ ). Actually, at redshifts  $z \lesssim 6$  the faint end of the luminosity/SFR functions has been recently explored, though still with large uncertainties, even down to  $M_{\text{UV}} \approx -13$  via gravitational lensing by foreground galaxy clusters [see 3, 4, 12, 50]. We have reported (but not used in the fit because of the still large systematic uncertainties) these data in Figure 1 to highlight that they are indeed consistent with the extrapolation of our SFR functions; specifically, the faint portion of the SFR function is seen to keep rising steeply with  $\alpha \lesssim 2$  out to  $z \lesssim 6$ .

## 2.2 Cosmic star formation rate density

Based on the star formation rate functions in the previous section, we can compute a star formation rate density:

$$\rho_{\text{SFR}}(z) = \int_{\dot{M}_\star^{\text{min}}}^{\infty} d \log \dot{M}_\star \frac{dN}{d \log \dot{M}_\star} \dot{M}_\star ; \quad (2.2)$$

Since the SFR function diverges at the faint end ( $\alpha \gtrsim 1$ ), the results are sensitive to the minimum SFR cutoff,  $\dot{M}_\star^{\text{min}}$ . Figure 2 shows the cosmic star formation rate based on integrating the UV-corrected SFR to three cut-offs:  $M_{\text{UV}} \approx -17$ , the observational limit of current blank field surveys. The outcome matches the determination by Madau & Dickinson [52, dotted line] and is in good agreement with the dust corrected data by Schiminovich et al. [77, cyan shaded area] at  $z \lesssim 4$  and by Bouwens et al. [11, cyan squares] at  $z \gtrsim 4$ . On the other hand, the cosmic SFR density from (dust-corrected) UV data is inconsistent with other datasets both at low and high redshift. Specifically, at redshift  $z \lesssim 4$  it falls short with respect to the multiwavelength determination by Hopkins & Beacom [37, orange shaded area] based on UV/optical, radio, H $\alpha$  and mid-IR 24  $\mu\text{m}$  data, to the far-IR measurements from *Herschel* by Magnelli et al. [54] and Gruppioni et al. [33, red shaded area], and by the recent estimate from deblended data from *Herschel*, JCMT/AzTEC and JCMT/SCUBA-2 in the GOODS field by Liu et al. [49]. At redshift  $z \gtrsim 4$  it underestimates the determinations based on stacking of far-IR data from *Herschel* by Rowan-Robinson et al. [76, red dots], the measurements from radio data by Novak et al. [64], and the estimates based on long GRB rates from *Swift* by Kistler et al. [42, 43]. This mostly reflects the fact, already mentioned above, that the UV-inferred SFR functions (even corrected for dust extinction by the UV slope) appreciably underestimate the number density of dusty galaxies with  $\dot{M}_\star \gtrsim 30 M_\odot \text{ yr}^{-1}$ .

Then we compute the cosmic SFR density exploiting our global SFR functions down to the same magnitude limit  $M_{\text{UV}}^{\text{min}} \approx -17$ . The outcome (solid line) is found to be in good agreement both with the Hopkins & Beacom [37], Gruppioni et al. [33] and Liu et al. [49] determinations at  $z \lesssim 4$ , with the stacked far-IR data by Rowan-Robinson et al. [76] at  $z \gtrsim 4$ . In Figure 2 we also show the outcomes when integrating our global SFR functions down to  $M_{\text{UV}}^{\text{lim}} \approx -13$  (dot-dashed line) and  $-12$  (dashed line); as we shall discuss in the next Section, these value are suggested by the recent data on the reionization history of the Universe in terms of electron scattering optical depth  $\tau_{\text{es}} \approx 0.058$  as measured by Planck Collaboration et al. [70].

### 2.3 Reionization history

The cosmic star formation history determines the cosmic ionization history. The cosmic ionization rate is proportional to cosmic SFR density:

$$\dot{N}_{\text{ion}} \approx f_{\text{esc}} k_{\text{ion}} \rho_{\text{SFR}} ; \quad (2.3)$$

here  $k_{\text{ion}} \approx 4 \times 10^{53}$  is the number of ionizing photons  $\text{s}^{-1} (M_{\odot}/\text{yr})^{-1}$ , with the quoted value appropriate for a Chabrier IMF, and  $f_{\text{esc}} \approx 1 - 20\%$  is the poorly constrained average escape fraction for ionizing photons from the interstellar medium of high-redshift galaxies [see 20, 58, 75]. Note that two other parameters implicitly entering in the expression  $\rho_{\text{SFR}}$  are the minimum UV limiting magnitude, and the faint-end slope of the SFR functions  $\alpha$  discussed at the end of Section 2.1.

The competition between ionization and recombination determines the evolution of the ionization state of the universe [see 25, 53]:

$$\dot{Q}_{\text{HII}} = \frac{\dot{N}_{\text{ion}}}{\bar{n}_{\text{H}}} - \frac{Q_{\text{HII}}}{t_{\text{rec}}} \quad (2.4)$$

Here  $\bar{n}_{\text{H}} \approx 2 \times 10^{-7} (\Omega_b h^2 / 0.022) \text{ cm}^{-3}$  is the mean comoving hydrogen number density. In addition, the recombination timescale reads  $t_{\text{rec}} \approx 3.2 \text{ Gyr} [(1+z)/7]^{-3} C_{\text{HII}}^{-1}$ , where the case B coefficient for an IGM temperature of  $2 \times 10^4 \text{ K}$  has been used; this timescale crucially depends on the clumping factor of the ionized hydrogen, for which a fiducial value  $C_{\text{HII}} \approx 3$  is usually adopted [see 67].

The electron scattering optical depth is proportional to the integrated electron density along the line-of-sight:

$$\tau_{\text{es}}(z) = c \sigma_{\text{T}} \bar{n}_{\text{H}} \int_t^{t_0} dt' f_e Q_{\text{HII}}(z') (1+z')^2; \quad (2.5)$$

here  $dt = \frac{dz}{H(z)}$  and  $H(z) = H_0 [\Omega_M (1+z)^3 + 1 - \Omega_M]^{1/2}$  is the Hubble parameter,  $c$  is the speed of light,  $\sigma_{\text{T}}$  the Thomson cross section and  $f_e$  the number of free-electrons per ionized hydrogen atom (assuming double Helium ionization at  $z \lesssim 4$ ).

Figure 3 shows the cosmic reionization history computed from our global SFR function integrated down to different  $M_{\text{UV}}^{\text{lim}}$ , on assuming a conservative value  $f_{\text{esc}} \approx 0.1$  for the escape fraction of ionizing photons. When adopting  $M_{\text{UV}}^{\text{lim}} \approx -13$ , the outcome (black dot-dashed line) agrees with the value of the optical depth for electron scattering  $\tau \approx 0.058$  recently measured by the *Planck* mission. For reference, the dotted line represents the optical depth expected in a fully ionized Universe up to redshift  $z$ ; this is to show that the bulk of the

reionization process occurred at  $z \sim 8 - 9$  and was almost completed at  $z \sim 6$  [see 78]. Note that from this perspective, the detailed behavior of the SFR functions at  $z \lesssim 6$  and at  $z \gtrsim 10$ , and the related ionizing background, are only marginally relevant. Remarkably, the evolution of the ionized fraction  $Q_{\text{HII}}$  illustrated in the inset is fully consistent with upper and lower limits from the plethora of independent observations collected by [75].

When adopting  $M_{\text{UV}}^{\text{lim}} \approx -17$ , that corresponds to the observational limits of current blank-field UV surveys at  $z \gtrsim 6$  (cf. Figure 2), the outcome on the optical depth (black solid line) touches the lower boundary of the  $1\sigma$  region allowed by *Planck* data, and the evolution of the  $Q_{\text{HII}}$  parameter is inconsistent with the aforementioned observational limits. At the other end, going much beyond  $M_{\text{UV}}^{\text{lim}} \approx -13$  is not allowed, since already for  $M_{\text{UV}}^{\text{lim}} \approx -12$  the resulting optical depth (black dashed line) touches the upper boundary of the  $1\sigma$  region from *Planck* data.

Note that these outcomes suffer to some extent of parameter degeneracy, as highlighted by the expression

$$f_{\text{esc}} k_{\text{ion}} C_{\text{HII}}^{-0.3} \Gamma[2 - \alpha; \dot{M}_{\star}^{\text{lim}} / \dot{M}_{\star, c}] \approx \text{const}, \quad (2.6)$$

where  $\Gamma[a; z] \equiv \int_z^\infty dx x^{a-1} e^{-x}$  is the incomplete  $\Gamma$ -function; the parameters involved are the escape fraction  $f_{\text{esc}}$ , the ionizing rate per unit SFR  $k_{\text{ion}}$  associated mainly to the IMF, the clumping factor  $C_{\text{HII}}$ , the faint-end slope of the SFR function  $\alpha$ , and the UV magnitude limit  $M_{\text{UV}}^{\text{lim}}$ . The strongest dependencies are on  $f_{\text{esc}}$  and on the limiting magnitude  $M_{\text{UV}}^{\text{lim}}$ . For example, to reproduce the *Planck* best estimate  $\tau_{\text{es}} \approx 0.058$  for  $M_{\text{UV}}^{\text{lim}} \approx -17$ , it would be necessary to force  $f_{\text{esc}}$  to implausible values  $\gtrsim 0.2$ ; at the other end, setting  $M_{\text{UV}}^{\text{lim}} \approx -12$  would require  $f_{\text{esc}} \lesssim 0.05$ , but at the cost of worsening the agreement with the observational constraints on  $Q_{\text{HII}}$ .

Thus the combined constraints on the cosmic reionization history from *Planck* and the cosmic SFR density measured at high redshifts  $z \gtrsim 6$  from galaxy surveys (see Figure 2) point toward a limiting UV magnitude  $M_{\text{UV}}^{\text{lim}} \approx -13$  and to an escape fraction  $f_{\text{esc}} \approx 10\%$ .



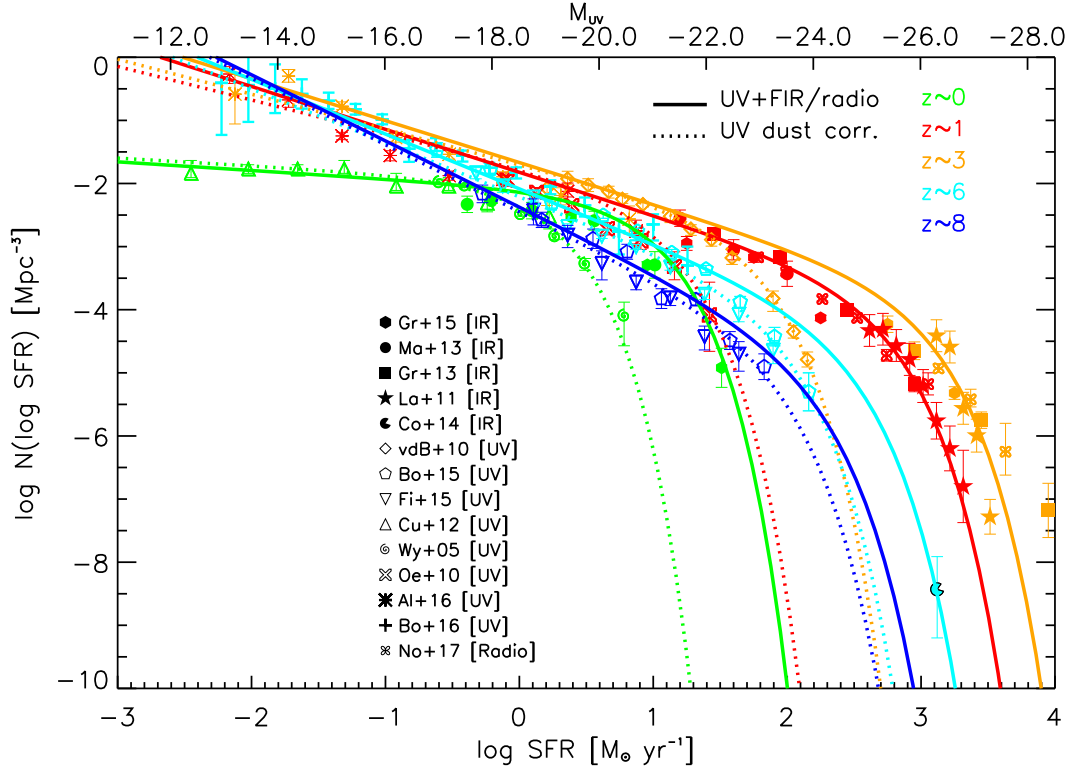


**Figure 1:** The SFR functions at redshifts  $z = 0$  (green), 1 (red), 3 (orange), 6 (cyan), and 8 (blue) determined according to the procedure by [55–57] and [44]. Solid lines refer to the rendition from UV (dust corrected according to standard prescriptions based on the UV slope) plus far-IR/radio data; dotted lines refer to the rendition from only (dust-corrected) UV data. UV data (open symbols) are from van der Burg et al. [86, diamonds], Bouwens et al. [11, pentagons], Finkelstein et al. [27, inverse triangles], Cucciati et al. [18, triangles], Wyder et al. [88, spirals], Oesch et al. [65, crosses], Alavi et al. [4, asterisks], Bouwens et al. [12, plus signs]; far-IR data from Gruppioni et al. [34, hexagons], Magnelli et al. [54, circles], Gruppioni et al. [33, squares], Lapi et al. [44, stars], and Cooray et al. [16, pacmans]; radio data from Novak et al. [64, clovers].



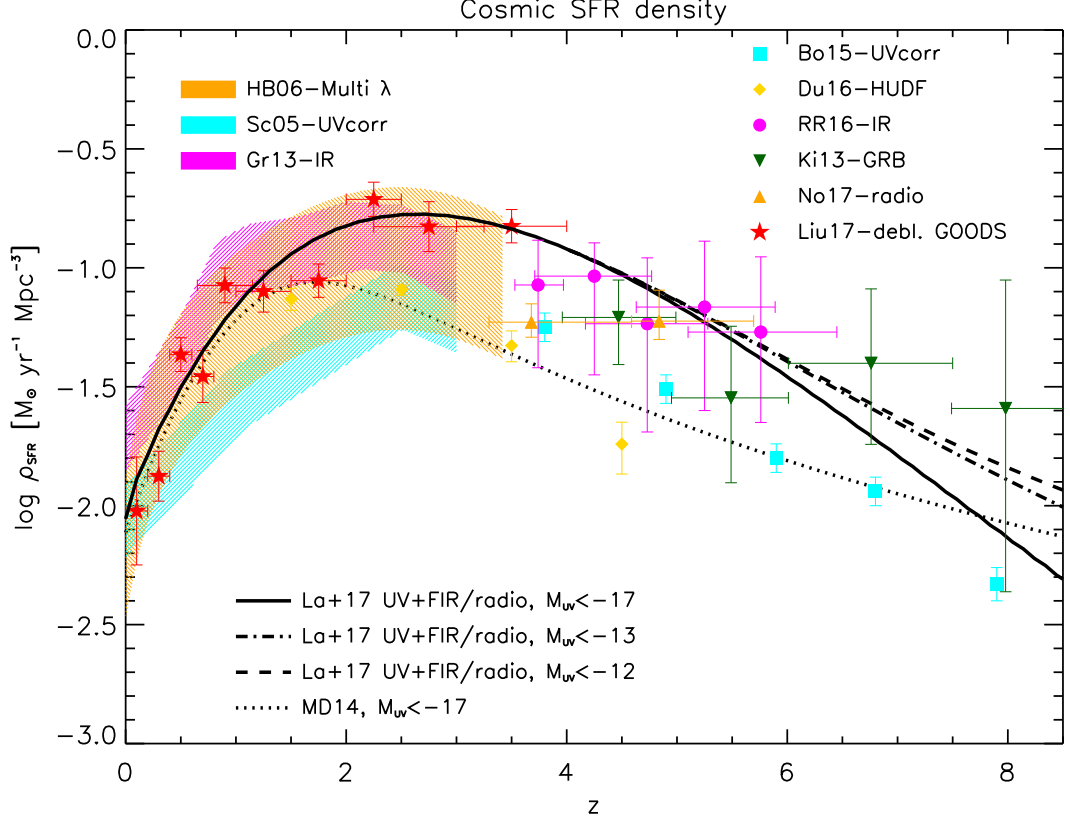


**Figure 2:** Cosmic SFR density as a function of redshift. The solid, dot-dashed, and dashed lines are our results on using the SFR functions from UV+far-IR/radio data presented in Figure 1, integrated down to a magnitude limit  $M_{\text{UV}} \lesssim -17$ ,  $-13$ , and  $-12$ , respectively. For comparison, the dotted line illustrates the determination by Madau & Dickinson [52] from dust-corrected UV data integrated down to a magnitude limit  $M_{\text{UV}} \lesssim -17$ . At  $z \lesssim 4$  data are from (dust-corrected) UV observations by Schiminovich et al. [77, cyan shaded area]; far-IR observations by Gruppioni et al. [33, magenta shaded area]; multiwavelength determination including UV, radio,  $\text{H}\alpha$ , and mid-IR  $24 \mu\text{m}$  data collected by Hopkins & Beacom [37, orange shaded area]; deblended far-IR/sub-mm data on the GOODS field by Liu et al. (2017; red stars). At higher redshifts  $z \gtrsim 4$ , we report the estimate of the SFR density inferred from (dust-corrected) UV data by Bouwens et al. [11, cyan squares], stacked IR data by Rowan-Robinson et al. [76, magenta circles], and long GRB rates by Kistler et al. [42, 43, green stars].

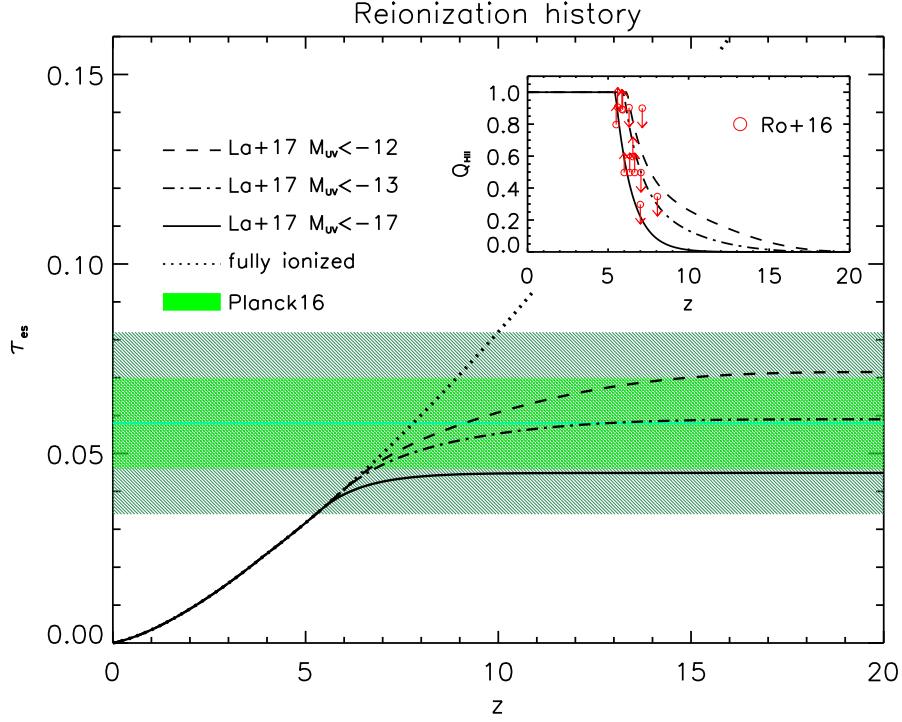


**Figure 3:** Reionization history of the universe, in terms of the redshift evolution of the optical depth  $\tau_{\text{es}}$  for electron scattering. Solid, dot-dashed and dashed lines illustrate the outcomes from our SFR functions integrated down to UV-magnitude limits  $M_{\text{UV}} \lesssim -17$ ,  $-13$ , and  $-12$ , respectively for an escape fraction of ionizing photons  $f_{\text{esc}} \approx 0.1$ . For reference, the dotted line refers to a fully ionized universe up to redshift  $z$ . The green line shows the measurement (with the  $1\sigma$  and  $2\sigma$  uncertainty regions highlighted by the dark and light green areas respectively) from Planck Collaboration et al. [70]. In the inset, the corresponding evolution of the ionized fraction  $Q_{\text{HII}}$  is plotted, together with upper and lower limits from various observations collected by Robertson et al. [75, empty circles].

Experiment name	Sensitivity $\Delta_T$ [ $\mu$ K arcminute]	$\theta_f$ [arcminute]
S4 (a)	1	1
S4 (b)	0.5	1
Litebird	1.8	16

**Table 1:**  $\theta_f$  is the full width half maxima of the incident beam. S4 (a) case is the configuration taken from the CMB S4 first science book [1] but as it is not still built up, just to be optimistic we are considering higher sensitive configuration in S4 (b) case.

### 3 CMB effects from Reionization

The cosmological reionization process makes its own signatures in the observed CMB sky. If reionization process did not take place, CMB photons could free-stream preserving their spectral shape originated at the time of recombination. The CMB spectral shape changes due to the y-type distortion by Comptonization process during reionization epoch [82]. The Compton y parameter is of the order of  $1.93 \times 10^{-7}$  for  $\tau = 0.058$  and electron temperature  $T_e = 2 \times 10^4$  K [19]. Rich groups at  $z \sim 1$  will produce a larger y distortion signal,  $\sim 1 - 2 \times 10^{-6}$  [35]. Due to the generation of free electrons along the line of sight, CMB photons scattered off by those electrons during the reionization epoch, and Thomson scattering generates new polarization at the large angular scales which adds up with the polarization induced at the last scattering surface. Primary CMB anisotropies are damped in all scales by a factor  $e^{-\bar{\tau}}$ , where  $\bar{\tau}$  is the mean reionization optical depth across the sky. Similar to CMB lensing, reionization also creates non-Gaussianity on CMB by correlating different Fourier modes. In this section we will discuss reionization morphology effects on the CMB by taking into account the reionization model discussed in the previous section and hereafter labelled as Empirical Extended Reionization Model (EERM). Throughout this paper we adopt two foreseen experiments representing the constraining capability of the CMB in the next decade. The first is represented by the network of ground based observatories mounting  $\sim 10^4$  detectors, known as stage-IV experiment (S4) and the second one is the LiteBIRD satellite from the Japanese space agency, optimized for large scale CMB polarization observations [59]. The main features of the probes in terms of angular resolution and sensitivity are summarized in Table 1.

#### 3.1 Sky-averaged effect

The sky-averaged reionization optical depth has been defined in Eq. (2.5) and can be also written as

$$\tau(z) = c\sigma_T \int_0^z \bar{n}_e(z') dz' \frac{dt}{dz'}, \quad (3.1)$$

Where  $c$  is the velocity of light in free space,  $\sigma_T$  is the Thomson scattering cross section and  $\bar{n}_e(z)$  is the mean free electron number density. As in Eq. (2.5) we express  $\bar{n}_e(z)$  in terms of present number density of protons  $n_{p0}$  and ionization fraction  $x_e(z)$  so that  $\bar{n}_e(z) = n_{p0}(1+z)^3 x_e(z)$  and  $dt/dz = [H(z)(1+z)]^{-1}$ , where  $H(z)$  is the Hubble parameter.

The tanh reionization model [46] is most commonly used to parametrize the reionization history of the universe and it is implemented inside Boltzmann equation solver codes like

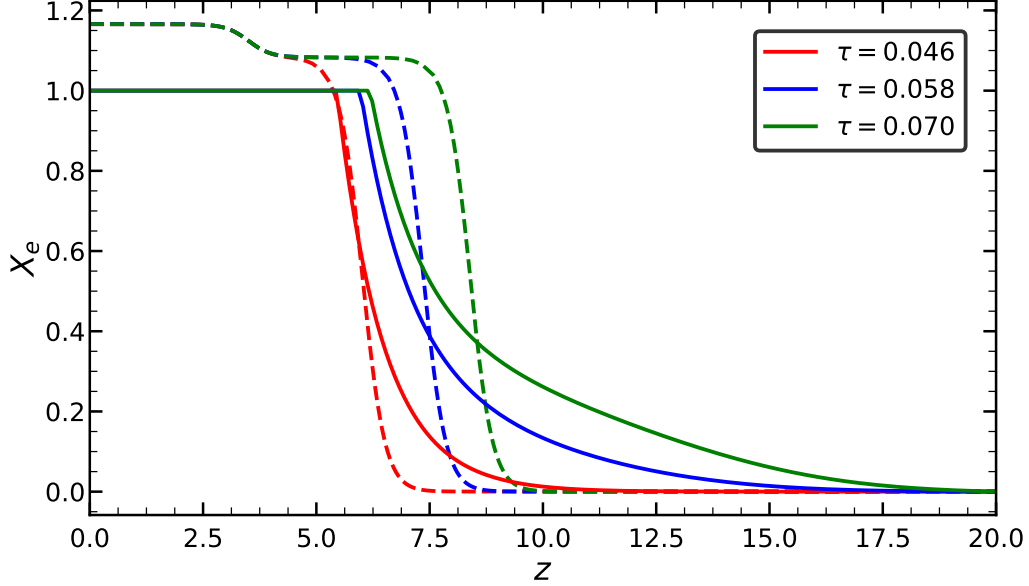


**Figure 4:** Solid lines represent the ionization history of the universe for three different optical depths considering EERM; the dashed lines are reionization histories calculated by the CLASS code using the tanh model for the same optical depths.

CAMB , CLASS [45, 46]:

$$x_e(z) = \frac{1}{2} \left[ 1 + \tanh \left( \frac{y_{re} - y(z)}{\Delta_y} \right) \right], \quad (3.2)$$

where  $y(z) = (1+z)^{\frac{3}{2}}$ ,  $y_{re} = y(z_{re})$  and  $\Delta_y = 1.5\sqrt{(1+z)}\Delta_z$ . Two free parameters of the model are the redshift  $z_{re}$  at which ionization becomes at the 50% level and  $\Delta_z$ , the width of the transition from neutral to fully ionizing state in redshift units.

We implement our reionization model, EERM by modifying CLASS code to check to which extent the EE and BB power spectrum sensitive to different ionization histories. In Figure 4 we compare the ionization history for EERM and the tanh reionization model corresponding to  $\tau = 0.070$  (green), 0.058 (blue) and 0.044 (red). EERM predicts more extended reionization process roughly in between the redshift range 16 to 7 corresponding to  $\tau = 0.058$  (solid blue line) whereas for the tanh case  $x_e$  changes more sharply in between redshift range 11 to 6 with fixed transition width  $\Delta_z = 0.5$  (dashed blue line). In Figure 5 EE spectra show the effect of the optical depth  $\tau$  as the amplitude of the bump increases with higher  $\tau$  value. Size of the horizon at the time of reionization is much larger than the horizon size at the time of last scattering, hence the  $\ell$  range at which the EE spectra become maximum is sensitive to mean redshift of reionization. The height of the reionization bump in the EE spectra is maximum around  $\ell \approx 4$  for EERM whereas for tanh reionization model it is around  $\ell \approx 3$ . The shift is due to a slight anticipation of the reionization process in the tanh model. Due to the extended reionization epoch there is excess power in  $5 \lesssim \ell \lesssim 12$  in EERM with respect to the tanh one.

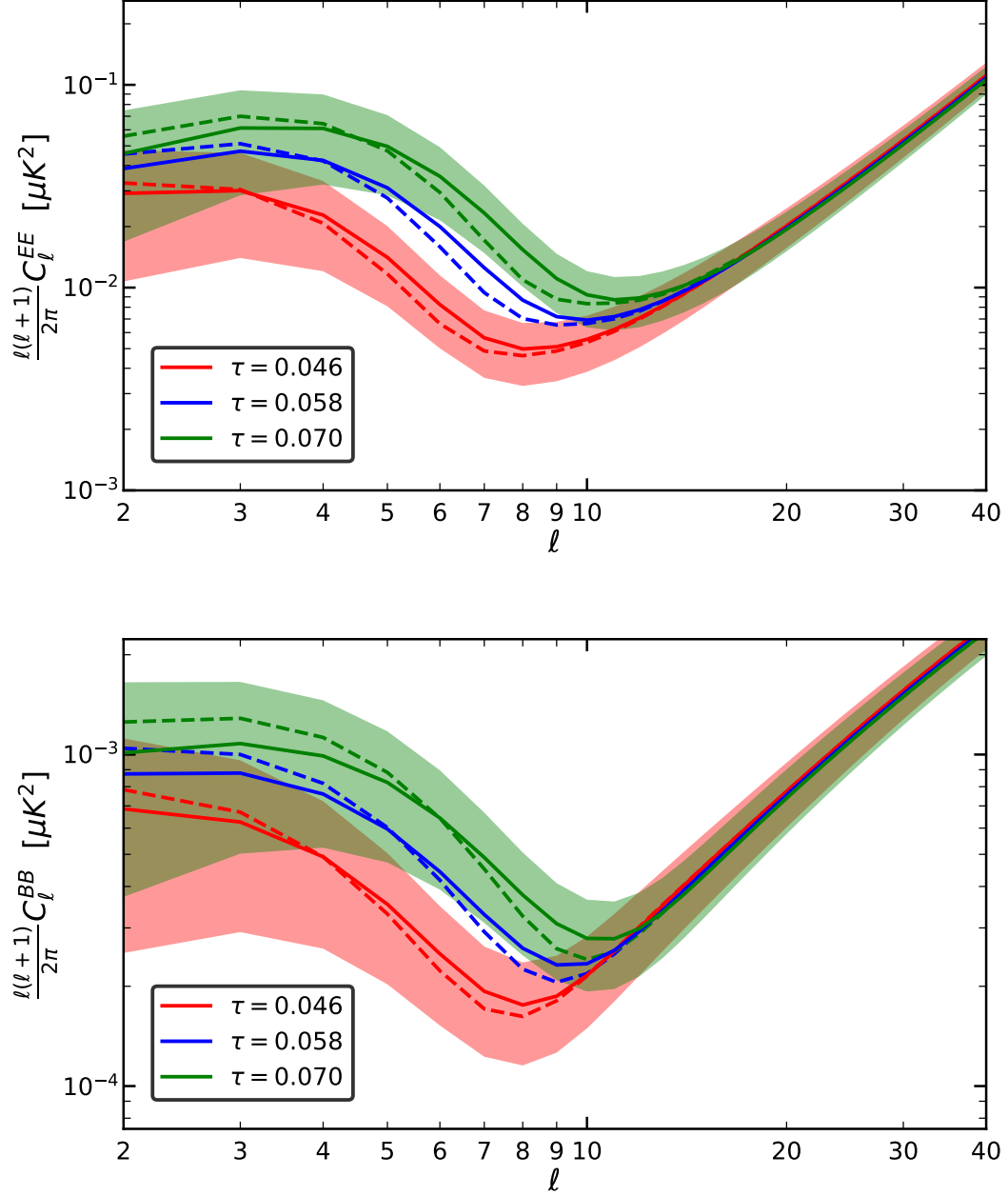


**Figure 5:** Upper panel: solid lines describe the EE power spectra for EERM and dashed lines are for the tanh case for three different optical depths. Green and red shaded areas show the  $1\sigma$  cosmic variance limit corresponding to the green ( $\tau = 0.07$ ) and the red ( $\tau = 0.046$ ) solid lines. In the bottom panel we plot the BB spectra for the same cases.

### 3.2 Patchy Reionization

We now focus on morphological aspects of the reionization process, the three most new effects with respect to those discussed previously are the following.

First, since we are considering the inhomogeneous reionization, optical depth  $\tau$  will be direction dependent quantity in the CMB sky, and the temperature and polarization anisotropy from the last scattering surface gets screened by a factor of  $e^{-\tau(\hat{n})}$  [21].

Second, new large scale polarization is generated as CMB local temperature quadrupole is scattered by the ionized regions, thereafter dubbed bubbles.

Third the peculiar motion of the ionized bubbles induces additional temperature fluctuations by KSZ during the epoch of reionization. KSZ effect due to patchy reionization will generate new power on small scales (around  $l \approx 3000$ ) [6, 80] in temperature power spectrum. In this paper we will not consider KSZ contribution as our interest is investigating the polarization anisotropy due to patchy reionization.

We assume the reionization happened by the percolation of ionized HII bubbles as well as the the growth in R [29, 87] inside the neutral intergalactic medium. We consider the size R of ionized bubbles following a log-normal distribution with two free parameters, the characteristic bubble size  $\bar{R}$  (in Mpc) and the standard deviation  $\sigma_{lnr}$ , given by

$$P(R) = \frac{1}{R} \frac{1}{\sqrt{2\pi\sigma_{lnr}^2}} \exp \left[ -\frac{\{\ln(R/\bar{R})\}^2}{2\sigma_{lnr}^2} \right]. \quad (3.3)$$

A bias  $b$  in the dark matter halo distribution will also influence the number density of ionized bubbles, but for simplicity we assume the bubble bias to be not evolving with redshift and independent of the bubble radius (in the redshift range of our interest); in this paper we use  $b = 6$ . In Figure 6 we show the radial distribution of ionized bubbles for EERM where we consider various values of  $\bar{R}$  and  $\sigma_{lnr}$ , be exploited in Section 5 to investigate how the reionization model affects the observables of patchy reionization. We stress that the radii distribution of bubbles strongly depends on the overall reionization history. For higher reionization optical depth w.r.t the present case, the distribution of bubbles has been studied numerically considering the complicated evolution of ionized bubbles during the reionization epoch[81]. We will comment more in this point in the conclusion section.

The merging of ionization bubbles creates fluctuations in ionization fraction,  $\delta x_e(\hat{\mathbf{n}}, \chi)$  over the mean ionization fraction  $\bar{x}_e(\chi)$  during the inhomogeneous reionization epoch, so that

$$x_e(\hat{\mathbf{n}}, \chi) = \bar{x}_e(\chi) + \delta x_e(\hat{\mathbf{n}}, \chi), \quad (3.4)$$

$$\tau(\hat{\mathbf{n}}, \chi) = c\sigma_T n_{p0} \int_0^\chi \frac{d\chi}{a^2} [\bar{x}_e(\chi) + \delta x_e(\hat{\mathbf{n}}, \chi)]. \quad (3.5)$$

In order to quantify the fluctuations in the ionization fraction, three dimensional power spectrum is expressed by the sum of the 1-bubble and 2-bubble contributions in total power spectrum corresponding to the scales in which  $r \ll R$  (1b) and  $r \gg R$  (2b), respectively. The main assumption for calculating the power spectrum of  $\delta x_e$  is that fluctuations in free electron density trace the fluctuations in dark matter density [29]. We take analytic expressions of 1b and 2b contributions from Dvorkin & Smith [22], given by:

$$P_{\delta x_e \delta x_e}^{1b}(k) = x_e(1 - x_e) [\alpha(k) + \beta(k)], \quad (3.6)$$

where the functional forms of  $\alpha(k)$  and  $\beta(k)$  are given by

$$\alpha(k) = \frac{\int dR P(R) [V(R) W(KR)]^2}{\int dR P(R) V(R)}, \quad (3.7)$$

$$\beta(k) = \int \frac{d^3 \mathbf{k}'}{(2\pi)^3} P(|\mathbf{k} - \mathbf{k}'|) \alpha(k'). \quad (3.8)$$

The volume of the bubble is  $V(R) = \frac{4}{3}\pi R^3$  and matter power spectrum is  $P(k)$ .  $W(kR)$  is the Fourier transform of the tophat window function with radius  $R$ , given by

$$W(kR) = \frac{3}{(kR)^3} [\sin(kR) - kR \cos(kR)]. \quad (3.9)$$

We adopt the approximation from [87] to calculate  $\beta(k)$  numerically, given by

$$\beta(k) = \frac{P(k) \sigma_R^2 \int dR P(R) V(R)}{[P^2(k) + \{\sigma_R^2 \int dR P(R) V(R)\}^2]^{1/2}}. \quad (3.10)$$

The 2b contribution is given by

$$P_{\delta x_e \delta x_e}^{2b}(k) = [(1 - x_e) \ln(1 - x_e) \gamma(k) - x_e]^2 P(k), \quad (3.11)$$

where  $\gamma(k)$  is defined by

$$\gamma(k) = b \cdot \frac{\int dR P(R) V(R) W(KR)}{\int dR P(R) V(R)}. \quad (3.12)$$

Therefore the total three dimensional power spectrum of  $\delta x_e$  can be written as

$$P_{\delta x_e \delta x_e}(k) = P_{\delta x_e \delta x_e}^{1b}(k) + P_{\delta x_e \delta x_e}^{2b}(k). \quad (3.13)$$

Now the optical depth power spectrum  $C_\ell^{\tau\tau}$  can be constructed from Eq.(3.13). In the flat sky approximation it can be written using Limber approximation as

$$C_\ell^{\tau\tau} = \sigma_T^2 n_{p0}^2 \int \frac{d\chi}{a^4 \chi^2} P_{\delta x_e \delta x_e} \left( \chi, k = \frac{\ell}{\chi} \right). \quad (3.14)$$

Inhomogeneous reionization is also the source of secondary anisotropies in the B mode polarization and the power spectrum can be connected also with  $P_{\delta x_e \delta x_e}$  [38, 62] as

$$C_\ell^{BB-patchy} = \frac{3\sigma_T^2 n_{p0}^2}{100} \int \frac{d\chi}{a^4 \chi^2} e^{-2\tau(\chi)} Q_{rms}^2 P_{\delta x_e \delta x_e} \left( \chi, k = \frac{\ell}{\chi} \right). \quad (3.15)$$

Here  $Q_{rms}$  is the r.m.s temperature of the local quadrupole and we used  $Q_{rms} = 22 \mu K$  during the patchy reionization epoch to calculate  $C_\ell^{BB-patchy}$ . In Figure 7 we compare BB spectra from patchy reionization with the foreseen sensitivities from S4 and LiteBIRD. As it can be seen, the signal is at the noise level in both cases, requiring additional steps for increasing the signal to noise ratio, described in the next section. We can see in the figure that S4(a) sensitivity is a bit lower in  $\ell \lesssim 200$  than the patchy BB signal both for  $\tau = 0.070$  and  $\tau = 0.058$  with  $\bar{R} = 10$  Mpc. On the other hand, the LiteBIRD sensitivity is a bit higher than patchy BB signal for the same configuration. S4(b) noise level is almost the same with respect to the Patchy BB signal even with  $\bar{R} = 5$  Mpc. This can be very useful in near future to constrain the morphology of the reionization by observing the patchy B mode signal.



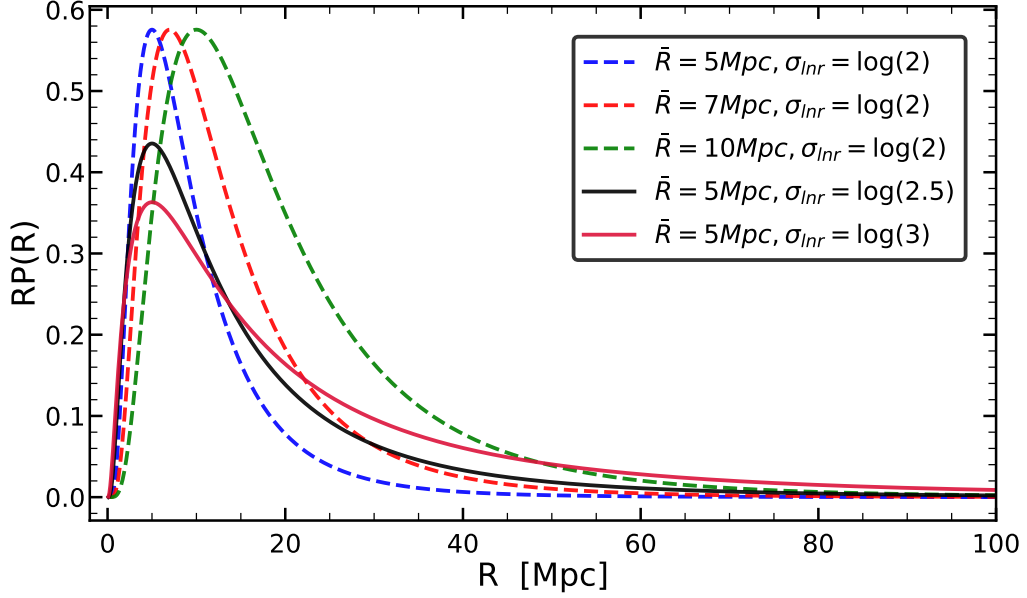


**Figure 6:** Distribution of bubble radius for different  $\bar{R}$  and  $\sigma_{Inr}$  as reported.

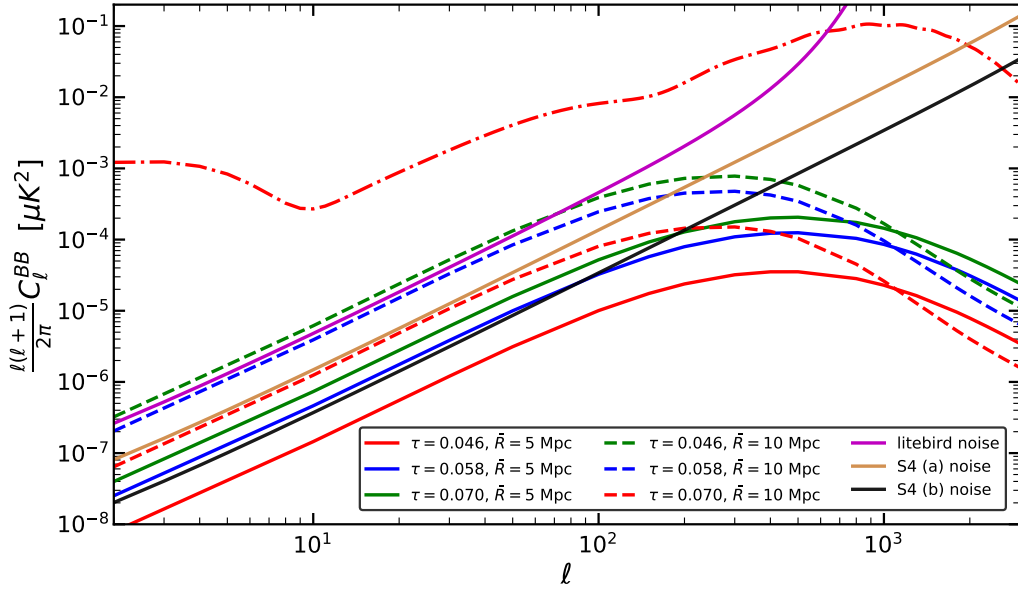


**Figure 7:** Green, Blue and red solid and dashed lines are B mode power spectrum generated due to patchy reionization for different values of  $\tau$  and  $\bar{R}$  as reported for EERM. We also report the BB spectrum for a cosmological model without patchy reionization, with  $\tau=0.058$  and tensor to scalar  $r=0.07$  (dotted dashed line). Purple, orange and black solid lines are the noise level for the experimental configurations of LiteBIRD, S4 (a) and S4(b) respectively.

#### 4 Reconstruction of $\tau$ along the line of sight

In Section 3.2 we discussed how patchy reionization induce additional structure in the observed CMB sky through  $\tau$  fluctuations. We consider that  $T$  and  $(Q \pm iU)$  are the temperature and polarization Stokes parameters before the start of reionization; then, at the end of the reionization, CMB temperature and polarization parameters will be changed as follow [22]:

$$T(\hat{\mathbf{n}}) = T_0(\hat{\mathbf{n}}) + \int \delta\tau T_1(\hat{\mathbf{n}}), \quad (4.1)$$

$$(Q \pm iU)(\hat{\mathbf{n}}) = (Q \pm iU)_0(\hat{\mathbf{n}}) + \int \delta\tau (Q \pm iU)_1(\hat{\mathbf{n}}), \quad (4.2)$$

Fluctuations in optical depth is given by:

$$\delta\tau = \int_{\chi_{start}}^{\chi_{end}} \frac{d\chi}{a^2} \delta x_e(\hat{\mathbf{n}}, \chi). \quad (4.3)$$

Where  $\chi_{start}$  and  $\chi_{end}$  are the comoving distances to the start and end of reionization respectively.  $T_0(\hat{\mathbf{n}})$  and  $(Q \pm iU)_0(\hat{\mathbf{n}})$  are the contributions coming from recombination and homogeneous reionization and  $T_1(\hat{\mathbf{n}})$  and  $(Q \pm iU)_1(\hat{\mathbf{n}})$  are the contribution from patchy reionization as defined in [22].

Separately we can write inhomogeneous screening terms as

$$T^{scr} = T_0(\hat{\mathbf{n}})e^{-\delta\tau(\hat{\mathbf{n}})}, \quad (4.4)$$

$$(Q \pm iU)^{scr} = (Q \pm iU)_0(\hat{\mathbf{n}})e^{-\delta\tau(\hat{\mathbf{n}})}, \quad (4.5)$$

accounting for the damping of anisotropies along the line of sight due to patchy reionization.

We now make a parallelism with the formalism applying to CMB lensing. The lensed field  $S_{len}(\hat{\mathbf{n}})$  is related with the unlensed field  $S_{unl}(\hat{\mathbf{n}})$  and the lensing potential  $\phi$  as [39]

$$S_{len}(\hat{\mathbf{n}}) = S_{unl}(\hat{\mathbf{n}}) + (\nabla\phi)\nabla S_{unl}(\hat{\mathbf{n}}) + O[(\nabla\phi)^2], \quad (4.6)$$

so, it modulates both the CMB polarization and temperature by correlating different Fourier modes. In flat sky approximation, after the lensing reconstruction method [22, 39], this correlation for patchy reionization can be written as

$$\langle S(\vec{\ell}_1)S'(\vec{\ell}_2) \rangle = (2\pi)^2 C_\ell^{SS'} \delta(\vec{L}) + f_{SS'}^\tau(\vec{\ell}_1, \vec{\ell}_2) [\delta\tau(\vec{L})], \quad (4.7)$$

where  $S, S'$  can be any combinations of T, E and B and  $\vec{L} = \vec{\ell}_1 + \vec{\ell}_2$ . We use only EB minimum variance quadratic estimator since it provides the highest signal to noise ratio to patchy reionization [22, 32].  $f_{EB}^\tau$  for flat sky is given by [81]

$$f_{EB}^\tau = (\bar{C}_{\ell_1}^{EE} - \bar{C}_{\ell_2}^{BB}) \sin 2(\phi_{\ell_1} - \phi_{\ell_2}), \quad (4.8)$$

where  $\bar{C}_{\ell_1}^{EE}$  and  $\bar{C}_{\ell_2}^{BB}$  are the EE and BB power spectra which include patchy reionization and  $\phi_\ell = \cos^{-1}(\hat{\mathbf{n}} \cdot \hat{\ell})$ . To satisfy Eq.(4.7) we can write minimum variance quadratic estimator of  $\tau(\vec{L})$  as

$$\hat{\tau}_{EB}(\vec{L}) = \tilde{N}_{EB}^\tau(\vec{L}) \int \frac{d^2\ell_1}{(2\pi)^2} \left[ E(\vec{\ell}_1)B(\vec{\ell}_2) \right] F_{EB}^\tau(\vec{\ell}_1, \vec{\ell}_2), \quad (4.9)$$

where  $\tilde{N}_{EB}^\tau(\vec{L})$  is the zeroth order bias for  $\tau$  reconstruction which can be thought in analogy to the  $N_{EB}^{(0)}$  bias for lensing potential reconstruction, given by

$$\tilde{N}_{EB}^\tau(\vec{L}) = \left[ \int \frac{d^2\vec{\ell}_1}{(2\pi)^2} f_{EB}^\tau(\vec{\ell}_1, \vec{\ell}_2) F_{EB}^\tau(\vec{\ell}_1, \vec{\ell}_2) \right]^{-1}. \quad (4.10)$$

The CMB instrumental noise power spectrum for a Gaussian symmetric beam can be written as

$$N_\ell^P = \Delta_P^2 \exp \left[ \frac{\ell(\ell+1)\Theta_f^2}{8 \ln 2} \right], \quad (4.11)$$

where  $\Delta_P$  is the noise of the detector for polarization in  $\mu K$ -arcmin; This is  $\sqrt{2}$  times bigger than the detector noise for temperature and  $\Theta_f$  is the full width half maxima of the beam in arcmin units.

In order to minimize the variance of  $\langle \hat{\tau}_{EB}(\vec{\ell}_1) \hat{\tau}_{EB}(\vec{\ell}_2) \rangle$ , the optimal form of filter  $F(\vec{\ell}_1, \vec{\ell}_2)$  for EB estimator is given by

$$F_{EB}^\tau(\vec{\ell}_1, \vec{\ell}_2) = \frac{f_{EB}^\tau(\vec{\ell}_1, \vec{\ell}_2)}{(C_{\ell_1}^{EB} + N_{\ell_1}^{EB})(2C_{\ell_2}^{EB} + N_{\ell_2}^{EB})}, \quad (4.12)$$

So that the expectation value of the estimator for  $\tau$  will reduce to

$$\langle \hat{\tau}_{EB}(\vec{\ell}_1) \hat{\tau}_{EB}(\vec{\ell}_2) \rangle = (2\pi)^2 \delta(\vec{\ell}_1, \vec{\ell}_2) \left[ C_L^{\tau\tau} + \tilde{N}_{EB}^\tau(\vec{L}) \right]. \quad (4.13)$$

We will use this technique in the next section to reconstruct the power spectrum of  $\tau$  using EERM prescription.

## 5 Detectability of the reionization angular power spectrum through $\tau$ reconstruction in S4 CMB experiments

In this section we discuss the capabilities of future CMB polarization experiments to detect the angular pattern of  $\tau$ . In order to do so we have modified the publicly available **Lenspix**<sup>9</sup> algorithm [47] to reconstruct  $\tau$  instead of the GL potential  $\phi$  following the algebra discussed in the previous Section. We focus on Eq.(3.14) in order to calculate the  $C_\ell^{\tau\tau}$  for our reionization model, EERM.

The uncertainty in the power spectrum of  $\tau$  comes from both the astrophysical modelling of the source of reionization and the uncertainty due to the modelling of reionization morphology. The first source of uncertainty is connected with the mean (sky averaged) optical depth  $\bar{\tau}$ , escape fraction  $f_{esc}$  and the source of reionization, which in our case is the star formation rate functions of high redshift galaxies. The morphology of reionization depends on the the bias factor, the mean radius of bubbles  $\bar{R}$  and also the spread of distribution of bubbles radii which is quantified by  $\sigma_{lnr}$  for a log normal distribution. We will consider the effects of  $\bar{R}$ ,  $\bar{\tau}$ , and  $\sigma_{lnR}$  uncertainties on the power spectrum of  $\tau$  for EERM, implementing a minimum variance quadratic estimator.

---

<sup>9</sup>cosmologist.info/lenspix

We calculate the Signal to Noise Ratio (SNR) to quantify the detectability of the patchy reionization:

$$\left(\frac{S}{N}\right) = \left[ \frac{f_{sky}}{2} \sum_{l_{min}}^{l_{max}} (2\ell + 1) \left( \frac{C_{\ell}^{\tau\tau}}{\bar{N}_{\ell}^{\tau\tau}} \right)^2 \right]^{1/2}. \quad (5.1)$$

Here  $f_{sky}$  is the observed sky fraction for a particular experiment. We mainly focus on instrumental specifications corresponding to S4, for which we use  $\Theta_f = 1$  arcmin and  $\Delta_T = 1$   $\mu K$ -arcmin, i.e  $\Delta_P = \sqrt{2}$   $\mu K$ -arcmin. We found that SNR for  $\tau$ -reconstruction does not strongly depend on  $\Theta_f$  as SNR changes a factor  $\approx 3$  when  $\Theta_f$  increased from  $1'$  to  $5'$  but SNR increases by a factor of  $\approx 80$  by the decrease of  $\Delta_T$  from 2  $\mu K$ -arcmin to 0.5  $\mu K$ -arcmin.

### 5.1 Dependence on $\bar{\tau}$

In Figure 8 we compute  $C_{\ell}^{\tau\tau}$  for three different optical depths, corresponding to the central value and  $\pm 1\sigma$  of the most recent measurements from Planck, and with fixed reionization parameters  $\bar{R} = 5$  Mpc and  $\sigma_{lnr} = \ln(2)$ . For  $\bar{\tau} = 0.044$ , the errors are too large at all scales for detectability, even for  $f_{sky} = 0.4$ . For  $\bar{\tau} = 0.070$  and  $0.058$ , an S4 experiment would be capable of probing  $\tau$  fluctuations in multipole range  $170 \lesssim \ell \lesssim 720$  and  $190 \lesssim \ell \lesssim 630$ , respectively, roughly corresponding to an interval from 1 to  $1/3$  of a degree. For a fixed detector sensitivity and beam resolving power, a measurement of the reionization morphology through  $C_{\ell}^{\tau\tau}$  is simply proportional to the value of mean optical depth  $\bar{\tau}$ . If LITEBIRD [59] achieves its sensitivity goal of  $\sigma(\bar{\tau}) = 0.002$ , then this would provide an important prior for detecting and interpreting the inhomogeneous reionization signal.

In Figure 9, we plot the binned and integrated SNRs. Depending on the values of  $\bar{\tau}$ , the CMB S4 specification should allow a  $1.4 - 5\sigma$  detection of the signal. For  $\tau = 0.44$ , the  $SNR < 1$  at all  $\ell$ s in the binned spectra. For  $\bar{\tau} = 0.7$  and  $\bar{\tau} = 0.58$ , S/N is greater than 1 in  $152 \lesssim \ell \lesssim 752$  and  $170 \lesssim \ell \lesssim 570$ , respectively.

### 5.2 Dependence on $\bar{R}$ and $\sigma_{lnr}$

The size and merger history of ionized bubbles is poorly understood. We consider the variation of reionization bubble radius  $\bar{R}$  and standard deviation of the log normal distribution of  $\sigma_{lnr}$ .

If the bubbles are larger ( $\bar{R} \approx 10$  Mpc), then the CMB S4 can probe  $\tau$  spectra in wide range of  $\ell$ s as error bars are small in  $52 \lesssim \ell \lesssim 852$  compared with the signal level. Whereas for  $\bar{R} = 7$  Mpc and  $\bar{R} = 5$  Mpc error bars are considerably larger than the signal level in the range of multipoles  $70 \lesssim \ell \lesssim 770$  and  $90 \lesssim \ell \lesssim 690$ , respectively.

In Figure 11 we can see that as  $\bar{R}$  increases, the integrated SNR also increases. In the range of  $5 \lesssim \bar{R} \lesssim 10$  Mpc, the signature of patchy reionization can be measured with  $4.3\sigma$  to  $19.2\sigma$  by covering 40% of the sky and  $4.8\sigma$  to  $21.3\sigma$  by observing 50% of the sky.

In Figure 12 we can see that for  $\sigma_{lnr} = \ln 3$  and  $\sigma_{lnr} = \ln 2.5$ ,  $C_{\ell}^{\tau\tau}$  can be measured in the range  $52 \lesssim \ell \lesssim 652$  and  $70 \lesssim \ell \lesssim 670$ . In the Figure 13, the integrated SNR reaches 267 which is much larger than the variation of  $\bar{R}$  and  $\bar{\tau}$ . Thus, due to the variation of  $\sigma_{lnr}$  in between  $\ln 2$  to  $\ln 3$ , the S4 specifications would allow to detect patchy reionization with a confidence ranging from  $4.8\sigma$  to  $267\sigma$ .

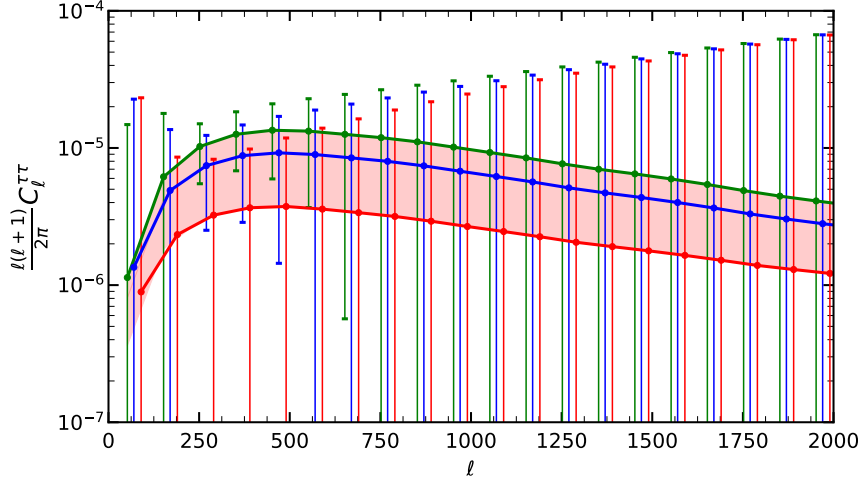


**Figure 8:** Green, blue and red solid lines represent the  $\tau$  angular power spectra corresponding to  $\bar{\tau} = 0.07, 0.058$  and  $0.044$ , respectively with  $\bar{R} = 5$  Mpc and  $\sigma_{lnr} = \ln(2)$ . We bin the each spectrum with  $\Delta\ell = 100$  and show the error bars accordingly. The error bars are located at  $\ell_{error} = (\ell_{min} + \frac{(2n-1)\Delta\ell}{2})$ , where  $\ell_{min}$  is the value of minimum  $\ell$  and  $n$  is the bin index; we fix  $\ell_{min} = 2$  (green curve), 20 (blue curve), 40 (red curve). Shaded pink area represents due to the  $1\sigma$  error of the  $\bar{\tau}$  measurement by Planck [70].

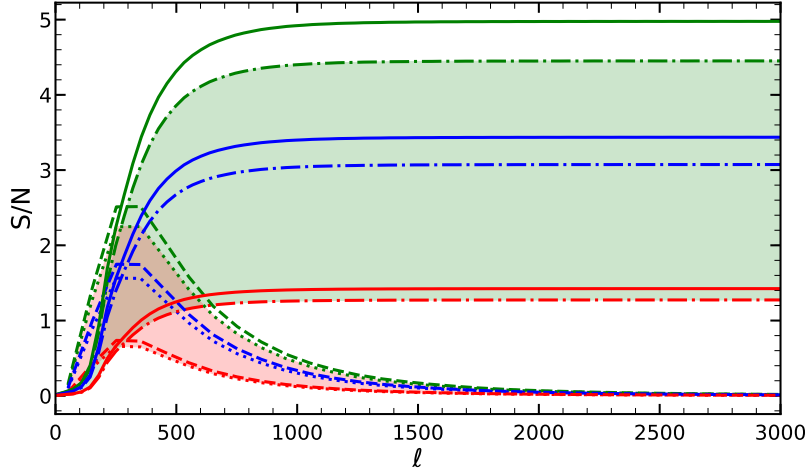


**Figure 9:** The binned and integrated SNR for the cases in Figure 9. Solid green, blue and red curve represent the integrated SNR for S4 sensitivity with  $f_{sky} = 0.5$  for  $\bar{\tau} = 0.07, 0.058, 0.044$ , respectively, while the dashed dotted curves are for  $f_{sky} = 0.4$ . Dashed green, blue and red lines represent the SNR in each bin for  $f_{sky} = 0.5$ , while dotted lines are for  $f_{sky} = 0.4$ .

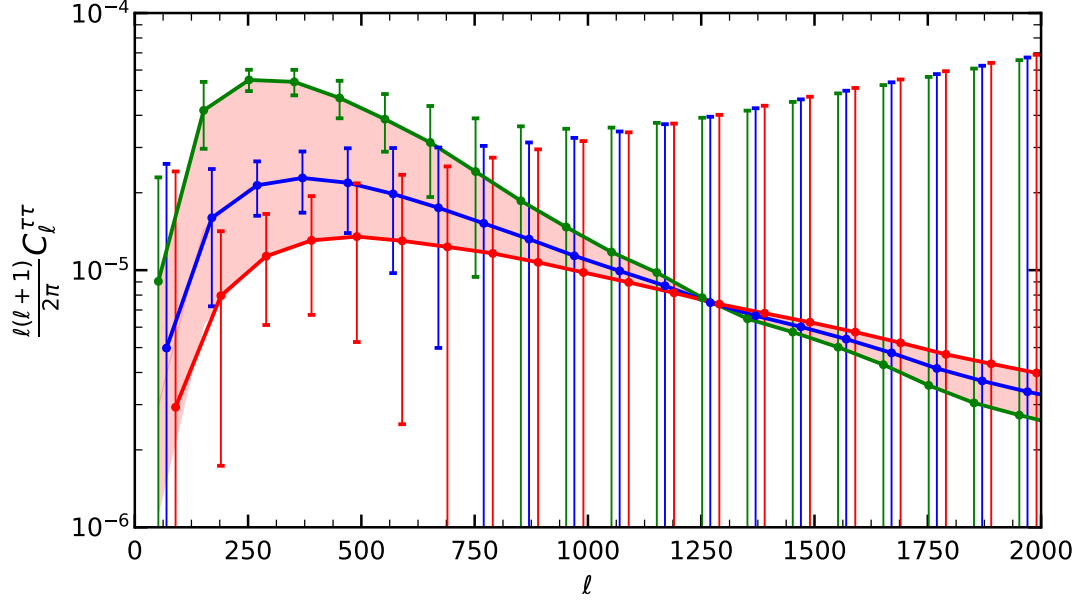


**Figure 10:** Green, blue and red solid lines are the  $\tau$  spectra with  $\bar{R} = 10, 7, 5$  Mpc, respectively, with  $\sigma_{lnr} = \ln 2$  for  $\bar{\tau} = 0.070$ . The binning scheme is as in the previous figures.

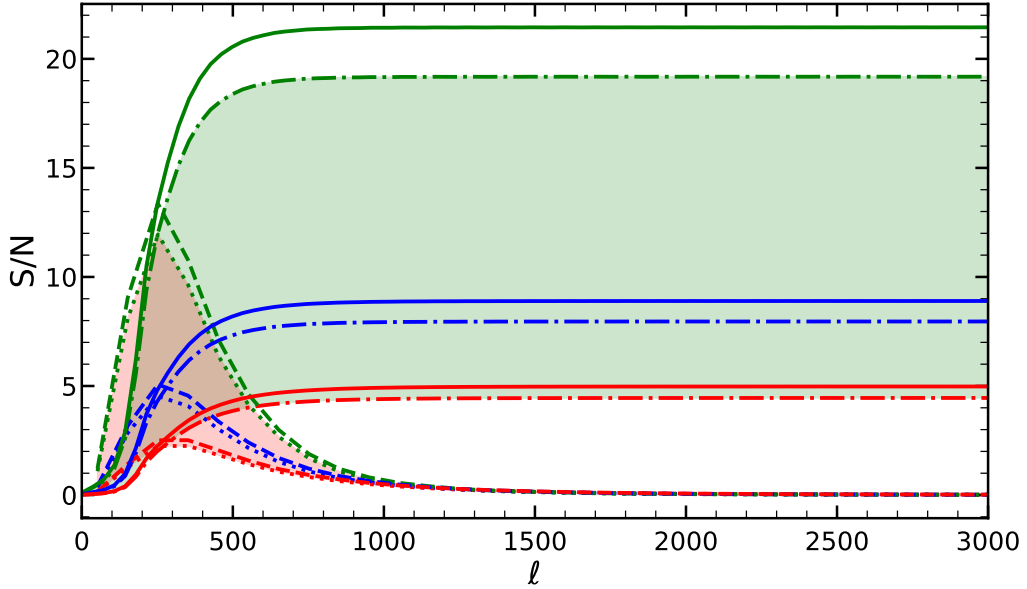


**Figure 11:** Binned and integrated SNR for the cases in Figure 10. Solid green, blue and red curve represent the integrated SNR for S4 sensitivity with  $f_{sky} = 0.5$  for three optical depths,  $\bar{\tau} = 0.07, 0.058, 0.044$ , respectively; dashed dot curves are for  $f_{sky} = 0.4$  with the same configuration. Dashed green, blue and red lines are SNR in each bin for  $f_{sky} = 0.5$ , while dotted lines for  $f_{sky} = 0.4$ .

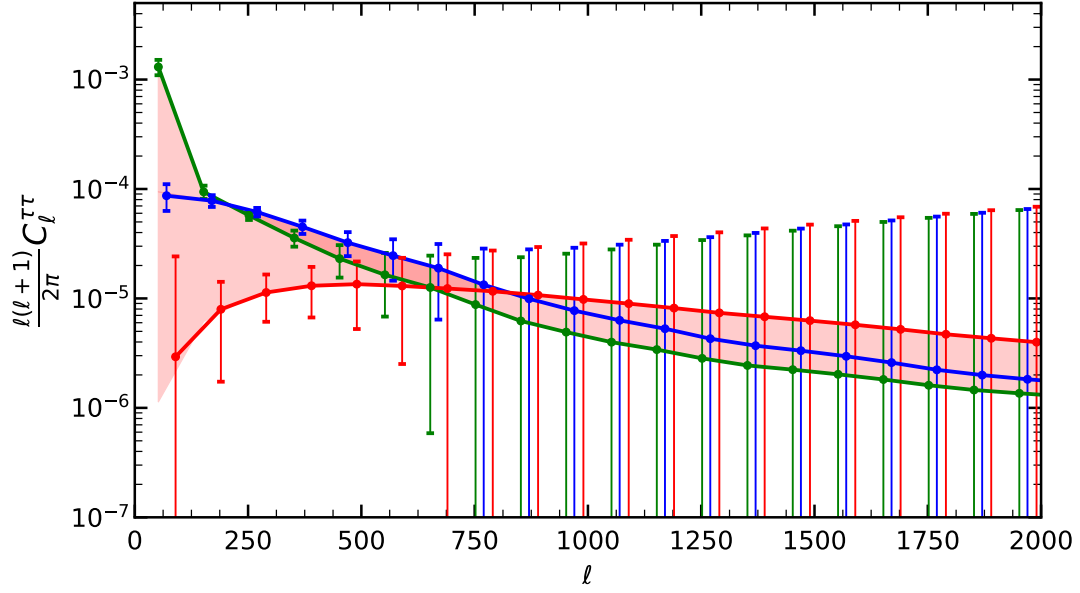


**Figure 12:** Green, blue and red solid lines are the  $\tau$  spectra for  $\sigma_{lnr} = \ln 3, \ln 2.5, \ln 3$ , respectively, with  $\bar{R} = 5$  Mpc for  $\bar{\tau} = 0.070$ . The binning scheme is as in the previous figures.

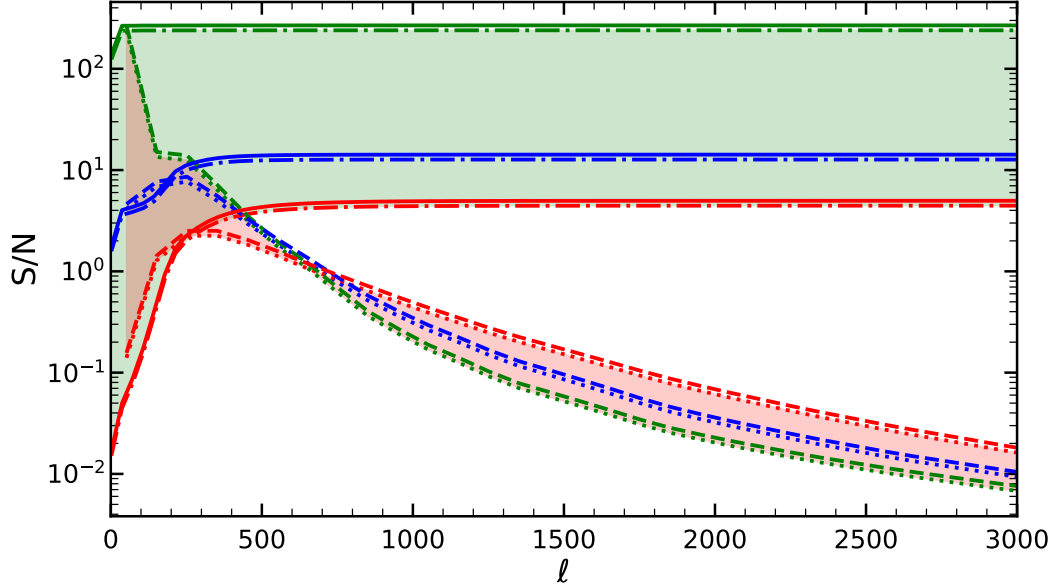


**Figure 13:** Binned and integrated SNR for the case in Figure 10. Solid green, blue and red curves represent the integrated SNR for S4 sensitivity with  $f_{sky} = 0.5$  for three optical depths  $\bar{\tau} = 0.07, 0.058, 0.044$ , respectively, and dashed dotted curves are for  $f_{sky} = 0.4$  with the same configuration. Dashed green, blue and red lines are SNR in each bin for  $f_{sky} = 0.5$ , while dotted lines for  $f_{sky} = 0.4$ .



## 6 Summary and Outlook

Cosmic reionization should be inhomogeneous with large ionized regions embedded in a shrinking neutral phase. This inhomogeneous reionization should produce a detectable signal. With its unprecedented sensitivity, CMB S4 should be capable of detecting the signal at a minimum, constraining the physics of reionization.

In this paper, we construct an ionizing background history that is based on recent astrophysical observations. We have adopted a simple parametrization of the size distribution of the early ionized regions; specifically we use a log-normal distribution in radius, characterized by a mean radius and a spread. The sky pattern of the reionization in such a picture is commonly known as patchy.

Following earlier works, we have implemented a procedure for the extraction of the patchy reionization signal analogue to the one exploited for CMB lensing and evaluated the signal to noise ratio achievable by CMB experiments reaching the S4 capabilities. The angular power spectrum is distributed broadly around the degree scale, with a long tail at higher multipoles. We have studied the amplitude of the signal as a function of the overall properties of the bubbles, and in particular on the abundance of the largest ones. If the bubble distribution has a tail with bubble size extending to tens of Mpc, then CMB S4 SNR could be in the many tens to hundreds.

Because our predicted signal is one order of magnitude larger than that estimated by Su et al. [81], lensing noise contamination should be a less relevant issue for us. Since the lensing behaviour is known for a given set of cosmological parameters, we can remove its contamination from our signal. These results demonstrate the capability of future CMB experiments to detect patchy reionization contribution to the CMB anisotropies.

## Acknowledgments

AR would like to thank Luigi Danese, Davide Poletti and Arnab Chakraborty for useful discussion throughout this project. This work partially supported by PRIN MIUR 2015 ‘Cosmology and Fundamental Physics: illuminating the Dark Universe with Euclid’, PRIN INAF 2014 ‘Probing the AGN/galaxy co-evolution through ultra-deep and ultra-high-resolution radio surveys’, and by the RADIOFOREGROUNDS grant (COMPET-05-2015, agreement number 687312) of the European Union Horizon 2020 research and innovation program.

## References

- [1] Abazajian, K. N., Adshead, P., Ahmed, Z., et al. 2016, ArXiv e-prints, arXiv:arxiv:1610.02743
- [2] Ahmed, Z., Amiri, M., Benton, S. J., et al. 2014, in Proceedings of the SPIE, Vol. 9153, Millimeter, Submillimeter, and Far-Infrared Detectors and Instrumentation for Astronomy VII, 91531N
- [3] Alavi, A., Siana, B., Richard, J., et al. 2014, ApJ, 780, 143
- [4] —. 2016, ApJ, 832, 56
- [5] Barkana, R., & Loeb, A. 2001, Physics Reports, 349, 125
- [6] Battaglia, N., Natarajan, A., Trac, H., Cen, R., & Loeb, A. 2013, ApJ, 776, 83
- [7] Becker, G. D., Bolton, J. S., & Lidz, A. 2015, Publications of the Astronomical Society of Australia, 32, e045

- [8] Benson, B. A., Ade, P. A. R., Ahmed, Z., et al. 2014, in *Proceedings of the SPIE*, Vol. 9153, *Millimeter, Submillimeter, and Far-Infrared Detectors and Instrumentation for Astronomy VII*, 91531P
- [9] Bouwens, R. J., Oesch, P. A., Illingworth, G. D., Ellis, R. S., & Stefanon, M. 2017, *ApJ*, 843, 129
- [10] Bouwens, R. J., Illingworth, G. D., Franx, M., et al. 2009, *ApJ*, 705, 936
- [11] Bouwens, R. J., Illingworth, G. D., Oesch, P. A., et al. 2015, *ApJ*, 803, 34
- [12] Bouwens, R. J., Aravena, M., Decarli, R., et al. 2016, *ApJ*, 833, 72
- [13] Bressan, A., Silva, L., & Granato, G. L. 2002, *A&A*, 392, 377
- [14] Chabrier, G. 2003, *Publications of the Astronomical Society of the Pacific*, 115, 763
- [15] Chornock, R., Berger, E., Fox, D. B., et al. 2013, *ApJ*, 774, 26
- [16] Cooray, A., Calanog, J., Wardlow, J. L., et al. 2014, *ApJ*, 790, 40
- [17] Coppin, K. E. K., Geach, J. E., Almaini, O., et al. 2015, *MNRAS*, 446, 1293
- [18] Cucciati, O., Tresse, L., Ilbert, O., et al. 2012, *A&A*, 539, A31
- [19] De Zotti, G., Negrello, M., Castex, G., Lapi, A., & Bonato, M. 2016, *JCAP*, 1603, 047
- [20] Dunlop, J. S., Rogers, A. B., McLure, R. J., et al. 2013, *MNRAS*, 432, 3520
- [21] Dvorkin, C., Hu, W., & Smith, K. M. 2009, *Phys. Rev. D*, 79, 107302
- [22] Dvorkin, C., & Smith, K. M. 2009, *Phys. Rev. D*, 79, 043003
- [23] Efstathiou, A., Rowan-Robinson, M., & Siebenmorgen, R. 2000, *MNRAS*, 313, 734
- [24] Fan, X., Strauss, M. A., Becker, R. H., et al. 2006, *AJ*, 132, 117
- [25] Ferrara, A., & Pandolfi, S. 2014, *ArXiv e-prints*, arXiv:arxiv:1409.4946
- [26] Filippini, J. P., Ade, P. A. R., Amiri, M., et al. 2010, in *Proceedings of the SPIE*, Vol. 7741, *Millimeter, Submillimeter, and Far-Infrared Detectors and Instrumentation for Astronomy V*, 77411N
- [27] Finkelstein, S. L., Ryan, Jr., R. E., Papovich, C., et al. 2015, *ApJ*, 810, 71
- [28] Fudamoto, Y., Oesch, P. A., Schinnerer, E., et al. 2017, *ArXiv e-prints*, arXiv:arxiv:1705.01559
- [29] Furlanetto, S., Zaldarriaga, M., & Hernquist, L. 2004, *Astrophys. J.*, 613, 1
- [30] Furlanetto, S. R., & Loeb, A. 2005, *ApJ*, 634, 1
- [31] Furlanetto, S. R., & Oh, S. P. 2005, *MNRAS*, 363, 1031
- [32] Gluscevic, V., Kamionkowski, M., & Cooray, A. 2009, *Phys. Rev. D*, 80, 023510
- [33] Gruppioni, C., Pozzi, F., Rodighiero, G., et al. 2013, *MNRAS*, 432, 23
- [34] Gruppioni, C., Calura, F., Pozzi, F., et al. 2015, *MNRAS*, 451, 3419
- [35] Hill, J. C., Battaglia, N., Chluba, J., et al. 2015, *Physical Review Letters*, 115, 261301
- [36] Hinshaw, G., Larson, D., Komatsu, E., et al. 2013, *ApJS*, 208, 19
- [37] Hopkins, A. M., & Beacom, J. F. 2006, *ApJ*, 651, 142
- [38] Hu, W. 2000, *Astrophys. J.*, 529, 12
- [39] Hu, W., & Okamoto, T. 2002, *ApJ*, 574, 566
- [40] Iliev, I. T., Pen, U.-L., Richard Bond, J., Mellema, G., & Shapiro, P. R. 2006, *New Astronomy Reviews*, 50, 909
- [41] Kennicutt, R. C., & Evans, N. J. 2012, *??jnlARA&A*, 50, 531

- [42] Kistler, M. D., Yüksel, H., Beacom, J. F., Hopkins, A. M., & Wyithe, J. S. B. 2009, *ApJL*, 705, L104
- [43] Kistler, M. D., Yüksel, H., & Hopkins, A. M. 2013, ArXiv e-prints, arXiv:arxiv:1305.1630
- [44] Lapi, A., Mancuso, C., Celotti, A., & Danese, L. 2017, *ApJ*, 835, 37
- [45] Lesgourgues, J. 2011, ArXiv e-prints, arXiv:arxiv:1104.2932
- [46] Lewis, A. 2008, *Phys. Rev. D*, 78, 023002
- [47] Lewis, A., Challinor, A., & Hanson, D. 2011, *JCAP*, 3, 018
- [48] Lidz, A., Oh, S. P., & Furlanetto, S. R. 2006, *ApJL*, 639, L47
- [49] Liu, D., Daddi, E., Dickinson, M., et al. 2017, ArXiv e-prints, arXiv:1703.05281
- [50] Livermore, R. C., Finkelstein, S. L., & Lotz, J. M. 2017, *ApJ*, 835, 113
- [51] Louis, T., Grace, E., Hasselfield, M., et al. 2017, *JCAP*, 6, 031
- [52] Madau, P., & Dickinson, M. 2014, *MNRAS*, 442, 415
- [53] Madau, P., Haardt, F., & Rees, M. J. 1999, *ApJ*, 514, 648
- [54] Magnelli, B., Popesso, P., Berta, S., et al. 2013, *A&A*, 553, A132
- [55] Mancuso, C., Lapi, A., Shi, J., et al. 2016, *ApJ*, 833, 152
- [56] —. 2016, *ApJ*, 823, 128
- [57] Mancuso, C., Lapi, A., Prandoni, I., et al. 2017, *ApJ*, 842, 95
- [58] Mao, J., Lapi, A., Granato, G. L., de Zotti, G., & Danese, L. 2007, *ApJ*, 667, 655
- [59] Matsumura, T., Akiba, Y., Borrill, J., et al. 2014, *Journal of Low Temperature Physics*, 176, 733
- [60] Meurer, G. R., Heckman, T. M., & Calzetti, D. 1999, *ApJ*, 521, 64
- [61] Mortlock, D. J., Warren, S. J., Venemans, B. P., et al. 2011, *Nature*, 474, 616
- [62] Mortonson, M. J., & Hu, W. 2007, *Astrophys. J.*, 657, 1
- [63] Natarajan, A., Battaglia, N., Trac, H., Pen, U.-L., & Loeb, A. 2013, *ApJ*, 776, 82
- [64] Novak, M., Smolčić, V., Delhaize, J., et al. 2017, *A&A*, 602, A5
- [65] Oesch, P. A., Bouwens, R. J., Carollo, C. M., et al. 2010, *ApJL*, 725, L150
- [66] Paranjape, A., & Choudhury, T. R. 2014, *MNRAS*, 442, 1470
- [67] Pawlik, A. H., Milosavljević, M., & Bromm, V. 2013, *ApJ*, 767, 59
- [68] Planck Collaboration, Ade, P. A. R., Aghanim, N., et al. 2016, *A&A*, 594, A13
- [69] Planck Collaboration, Adam, R., Aghanim, N., et al. 2016, *A&A*, 596, A108
- [70] —. 2016, *A&A*, 596, A108
- [71] Reddy, N. A., Kriek, M., Shapley, A. E., et al. 2015, *ApJ*, 806, 259
- [72] Reichborn-Kjennerud, B., Aboobaker, A. M., Ade, P., et al. 2010, in *Proceedings of the SPIE, Vol. 7741, Millimeter, Submillimeter, and Far-Infrared Detectors and Instrumentation for Astronomy V*, 77411C
- [73] Riechers, D. A., Leung, T. K. D., Ivison, R. J., et al. 2017, ArXiv e-prints, arXiv:arxiv:1705.09660
- [74] Robertson, B. E., Ellis, R. S., Dunlop, J. S., McLure, R. J., & Stark, D. P. 2010, *Nature*, 468, 49
- [75] Robertson, B. E., Ellis, R. S., Furlanetto, S. R., & Dunlop, J. S. 2015, *ApJL*, 802, L19

- [76] Rowan-Robinson, M., Oliver, S., Wang, L., et al. 2016, MNRAS, 461, 1100
- [77] Schiminovich, D., Ilbert, O., Arnouts, S., et al. 2005, ApJL, 619, L47
- [78] Schultz, C., Oñorbe, J., Abazajian, K. N., & Bullock, J. S. 2014, MNRAS, 442, 1597
- [79] Silva, L., Granato, G. L., Bressan, A., & Danese, L. 1998, ApJ, 509, 103
- [80] Smith, K. M., & Ferraro, S. 2017, Phys. Rev. Lett., 119, 021301
- [81] Su, M., Yadav, A. P. S., McQuinn, M., Yoo, J., & Zaldarriaga, M. 2011, ArXiv e-prints, arXiv:arxiv:1106.4313
- [82] Sunyaev, R. A., & Khatri, R. 2013, International Journal of Modern Physics D, 22, 1330014
- [83] Suzuki, A., Ade, P., Akiba, Y., et al. 2016, Journal of Low Temperature Physics, 184, 805
- [84] The Polarbear Collaboration: P. A. R. Ade, Akiba, Y., Anthony, A. E., et al. 2014, ApJ, 794, 171
- [85] Totani, T., Aoki, K., Hattori, T., et al. 2014, Publications of the Astronomical Society of Japan, 66, 63
- [86] van der Burg, R. F. J., Hildebrandt, H., & Erben, T. 2010, A&A, 523, A74
- [87] Wang, X., & Hu, W. 2006, ApJ, 643, 585
- [88] Wyder, T. K., Treyer, M. A., Milliard, B., et al. 2005, ApJL, 619, L15
- [89] Zavala, J. A., Montaña, A., Hughes, D. H., et al. 2017, ArXiv e-prints, arXiv:arxiv:1707.09022